Direct electrochemical generation of supercooled sulfur microdroplets well below their melting temperature

Nian Liu[a,b,c,1,2], Guangmin Zhou[b,1], Ankun Yang[b], Xiaoyun Yu[b], Feifei Shi[b], Jie Sun[b], Jinsong Zhang[b], Bofei Liu[b], Chun-Lan Wu[b], Xinyong Tao[b,d], Yongming Sun[b], Yi Cui[b,e,2], and Steven Chu[a,f,2]

[a]Department of Physics, Stanford University, Stanford, CA 94305; [b]Department of Materials Science and Engineering, Stanford University, Stanford, CA 94305; [c]School of Chemical & Biomolecular Engineering, Georgia Institute of Technology, Atlanta, GA 30332; [d]College of Materials Science and Engineering, Zhejiang University of Technology, 310014 Hangzhou, China; [e]SLAC National Accelerator Laboratory, Stanford Institute for Materials and Energy Sciences, Menlo Park, CA 94025; and [f]Department of Molecular and Cellular Physiology, Stanford University, Stanford, CA 94305

Contributed by Steven Chu, November 30, 2018 (sent for review March 29, 2018; reviewed by Jun Liu and David A. Weitz)

Supercooled liquid sulfur microdroplets were directly generated from polysulfide electrochemical oxidation on various metal-containing electrodes. The sulfur droplets remain liquid at 155 °C below sulfur's melting point (T_m = 115 °C), with fractional supercooling change ($T_m - T_{sc}$)/T_m larger than 0.40. *In operando* light microscopy captured the rapid merging and shape relaxation of sulfur droplets, indicating their liquid nature. Micropatterned electrode and electrochemical current allow precise control of the location and size of supercooled microdroplets, respectively. Using this platform, we initiated and observed the rapid solidification of supercooled sulfur microdroplets upon crystalline sulfur touching, which confirms supercooled sulfur's metastability at room temperature. In addition, the formation of liquid sulfur in electrochemical cell enriches lithium-sulfur-electrolyte phase diagram and potentially may create new opportunities for high-energy Li-S batteries.

supercooled liquids | liquid sulfur droplets | in situ optical microscopy | Li-S batteries | crystallization

Supercooling, a phenomenon that a substance stays in liquid form well below its melting point, exists in stratiform and cumulus clouds, allows plants and animals to survive extremely cold weather (1, 2), and has been utilized broadly in nanomaterial synthesis (3), transplant organ preservation (4), heat-free soldering (5), etc. While the theories and properties of supercooling have been studied extensively (6–10), the production of supercooled liquids has been limited to varying the temperature or pressure: a solid is first melted or vaporized and then cooled to below its melting point (11, 12), or an amorphous solid is heated (13), or a solid is decompressed from high pressure (e.g., gigapascal) (14). Also, precise control of the supercooled liquid droplet size and location requires complex setup (15, 16), such as aerodynamic levitation and microfluidics.

Electrochemically oxidizing polysulfide (S_x^{2-}, x = 3–8) on an electrode surface produces elemental sulfur (Eq. **1**). Different from conventional thermal vapor condensation, the electrochemical process generates sulfur directly at constant temperature, with precise control of the formation speed, and in the vicinity of electrode.

$$S_x^{2-}\text{-}2e^- \rightarrow x/8\ S_8,\ x=3\text{-}8. \quad [1]$$

Since supercooling has been shown to be substrate dependent (17), we investigated whether supercooled sulfur could be directly formed by the electrochemical method at temperature well below its melting point and constant ambient pressure. In this work, we show that liquid sulfur droplets do not wet certain metal electrodes when the chance that the surface interface can induce crystallization of S_8 molecules is minimized. More generally, the electrochemical condensation of molecules dissolved in solution into a liquid state introduces a way to produce supercooled substances with unprecedented level of control. In addition, the potential of lithium-sulfur electrochemistry for high-energy density batteries beyond conventional Li-ion batteries calls for fundamental understanding of sulfur electrochemistry (18–20). Substrates such as nickel metal and nickel-containing compounds have been reported to be beneficial for both the areal current density and areal capacity of sulfur electrode (21, 22), yet the mechanism remains unclear possibly due to a lack of tools to study this process in real time, real electrolyte, and high spatial resolution.

Probing sulfur electrochemistry has multiple challenges that include: (*i*) sulfur and its reduced species are extremely sensitive to vacuum, electron beam irradiation (23), and X-ray irradiation, which limits the diagnostic tools one can use; (*ii*) sulfur has a large family of intermediate species connected by interwoven reaction pathways, which could be easily disturbed by added indicators or labels; and (*iii*) the materials easily change upon removing from native electrolyte, hence often requiring *in operando* study.

Here we combine dark-field light microscopy (DFLM) and a planar electrochemical cell fabricated on a glass slide to visualize

PHYSICS

Significance

Since the first discovery of supercooling in 1724, the study of supercooled matter has been mainly limited to varying temperature or pressure. Here we demonstrate an electrochemical approach to generate and observe supercooled sulfur. Our methodology combines dark-field microscopy, a transparent electrochemical cell, and a fast camera to visualize the process at single microdroplet with millisecond time resolution. This platform may open up opportunities for studying supercooled liquids as the droplets approach either homogeneous nucleation to the crystalline state or enter into the glass transition. Relevant to understanding lithium-sulfur battery chemistry, liquid sulfur is observed to form in the electrochemical cell and elucidates a long-debated reaction pathway for sulfur redox reaction in this environment.

Author contributions: N.L., G.Z., Y.C., and S.C. designed research; N.L. and G.Z. performed research; N.L., G.Z., A.Y., X.Y., F.S., J.S., J.Z., B.L., C.-L.W., X.T., Y.S., Y.C., and S.C. analyzed data; and N.L., G.Z., Y.C., and S.C. wrote the paper.

Reviewers: J.L., Pacific Northwest National Laboratory; and D.A.W., Harvard University.

The authors declare no conflict of interest.

[1]N.L. and G.Z contributed equally to this work.

[2]To whom correspondence may be addressed. Email: nian.liu@chbe.gatech.edu, yicui@stanford.edu, or schu@stanford.edu.

This article contains supporting information online at www.pnas.org/lookup/suppl/doi:10.1073/pnas.1817286116/-/DCSupplemental.

Published online January 2, 2019.

sulfur electrochemistry *in operando* (Fig. 1*A*). Pictures of the electrochemical cell are shown in *SI Appendix*, Fig. S1. Visible light is a benign probe which allows noninvasive study in native ether-based liquid electrolyte, while dark-field illumination was used to enhance the sensitivity to small features on a flat background. Lithium polysulfide (Li_2S_8) was dissolved in dioxolane (DOL) and dimethyl ether (DME) and served as the electrolyte and sulfur source. A Ni grid electrode (1 μm in line width, 50 nm in height) was deposited on a glass substrate via e-beam lithography and evaporation (Fig. 1 *B* and *C* and *SI Appendix*, Fig. S2), while Li metal placed on the same plane was the counter/reference electrode. During galvanostatic charging/discharging at room temperature (Fig. 1*D*), sulfur deposits on/strips from the working electrode, while DFLM images of a 180 μm × 135 μm region on the surface of the Ni substrate were captured at 1 frame per second simultaneously (Fig. 1 *E*–*I*). A white light source and a three-color-channel complementary metal-oxide semiconductor (CMOS) camera were used to record color information. Using this technique, we are able to directly observe multiple phenomena in lithium-sulfur (Li-S) batteries, including the electrochemical generation of metastable liquid sulfur at room temperature, rapid solidification of sulfur droplets upon crystal nucleation, and sulfur deposition/stripping via solution mechanism.

During electrochemical cycling, liquid-like sulfur microspheres form on Ni grids toward the end of charging (formation starts at ~2.8 V when applying 0.05 mA), and reversibly reduce into soluble polysulfide upon discharging (Fig. 1 *E*–*I* and Movie S1 for a recording of the droplet dynamics). Well-separated nickel grids allow sulfur microspheres to be individually resolved and monitored. The microspheres are spherical, semitransparent to light, and form over the entire surface of nickel grid electrode (Movie S2). As they grow larger and approach each other, neighboring droplets occasionally merge into larger droplets that relax rapidly to a spherical shape to minimize surface energy (Fig. 1 *J* and *K*). Similar liquid sulfur droplets also form on flat Ni film (Movie S3).

Assuming perfect spheres for these droplets both before and after merging, we find the total volume is conserved (*SI Appendix*, Fig. S3). The dynamics of the merging events, which

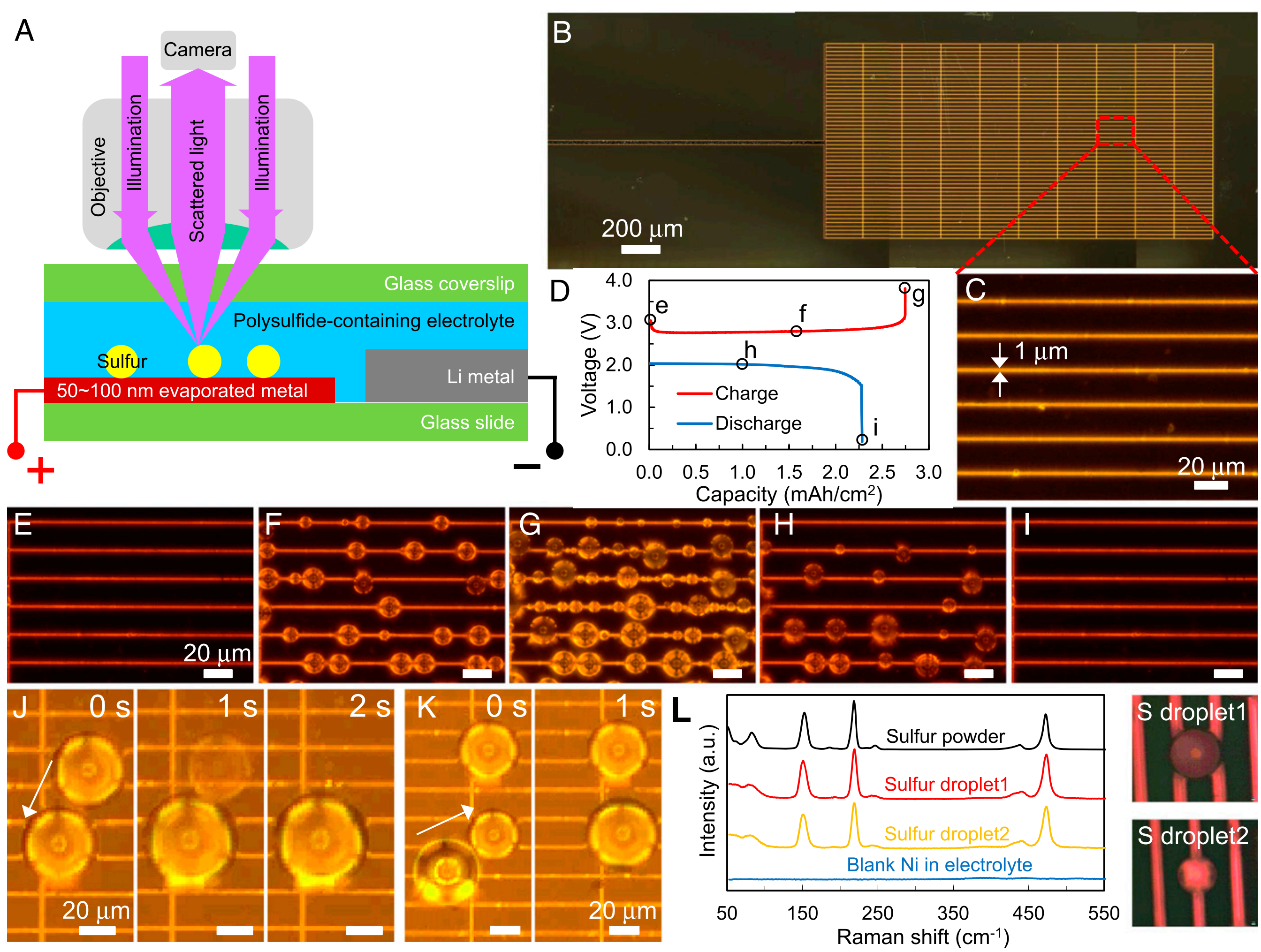

Fig. 1. *In operando* observation of supercooled sulfur generated electrochemically at room temperature. (*A*) Schematic of the electrochemical cell design that allows *in operando* DFLM observation. (*B* and *C*) DFLM images of the nickel metal grid (50 nm thick, 1 μm wide) fabricated on glass slide as a substrate for the electrochemical cell. Bright lines are nickel, elsewhere is glass. (*D*–*I*) Voltage profile of the cell (*D*) and corresponding time-lapse DFLM images (*E*–*I*) showing the formation and dissolution of supercooled sulfur droplets. (*J* and *K*) Two sets of time-lapse images showing rapid merging of neighboring droplets and relaxation to spherical shape within 1 s, indicating the liquid nature of sulfur. (*L*) In situ Raman spectra of supercooled sulfur droplets. (*Right*) Corresponding bright-field light microscopy images captured by the Raman microscope are shown (magnification: 50×). The spectra match that of solid S_8 powder, and the signals are not from electrolyte or substrate.

indicate liquid-like behavior of the sulfur microspheres, is not resolved with an image capture rate of 1 frame per second. Time-lapse images captured using an optical microscope equipped with a high-speed camera show that the merging is composed of two steps: The actual merging finishes within 0.2 ms, and the shape relaxation of merged droplets finishes in a few milliseconds (*SI Appendix*, Figs. S4 and S5).

To confirm the chemical composition of microdroplets, micro-Raman spectroscopy was performed on the same sealed electrochemical cell. The Raman spectrometer had sufficient spatial resolution to collect spectra on individual sulfur microdroplets (Fig. 1*L*). The spectra of the droplets match that of solid sulfur powders but not polysulfides (24), indicating the liquid droplets are chemically cyclosulfur (S_8). Eutectic alloys of sulfur with other elements can significantly alter the freezing temperature, but the Raman spectra rule out this possibility. On the other hand, it is well known that small amounts of impurities serve as heterogeneous nucleation sites that limit the degree of supercooling (25–27). Sulfur in its molten state is also known to form polymeric chains, but earlier Raman spectroscopy investigations of the polymerization of S_8 monomers into higher-order S_n polymers concluded that polymerization occurs at temperatures greater than 140 °C (28).

The interior temperature of the electrochemical cell is unlikely to be noticeably higher than room temperature under xenon lamp illumination, since liquid electrolyte has good dissipation of heat. Also, we do not observe the melt of solid sulfur under the same conditions. The constant contrast in the background of the movie does not change over time and may possibly be due to dust or surface roughness of the substrate. We do not observe large morphological changes corresponding to the formation of Li_2S at the end of discharge, except some small diffraction-limited spots (Movie S3).

In addition to nickel, these supercooled liquid sulfur microdroplets electrochemically form on various other metal-containing substrates, including palladium, platinum, indium tin oxide (ITO), and cobalt sulfide (CoS_2) (Fig. 2*A*, *SI Appendix*, Figs. S6 and S7, and Movies S4–S7). In contrast, carbon substrate (polished glassy carbon) leads to the formation of irregular crystalline solid sulfur particles that do not undergo significant changes when contacting with each other (Fig. 2*B* and Movie S8). Therefore, the electrochemical formation of supercooled sulfur is both generic and substrate dependent. It should be noted that the supercooling reported here is unlikely to stem from a size effect. Liquid-like behaviors have been shown to accompany extremely small (<10 nm) particles (29), but the droplets reported here are micrometer scale, whose melting point is close to bulk according to the Gibbs–Thomson equation (30).

Although it was reported earlier that liquid sulfur condensed from hot vapor could remain liquid state at room temperature when the size of droplet is smaller than a millimeter (11), the electrochemical pathway reported here can generate supercooled liquid sulfur at constant temperature, since the electrochemical potential introduces another thermodynamic variable that is able to alter the relative free energy between polysulfides in electrolyte (analogous to sulfur in a gaseous state) and condensed S_8 on the electrode.

There are several factors that facilitate the formation of supercooled sulfur in an electrochemical cell. First, the location, size, and growth rate of the sulfur droplets can be well controlled by the electrode patterning, capacity, and current. Relatively large current (0.05 mA) and short duration (6 min) produce droplets smaller than 10 μm (*SI Appendix*, Fig. S8), which helps them to maintain supercooled liquid state at room temperature. Second, the supercooled sulfur here has nearly 180° contact angle with the metal-containing solid substrates, which minimizes its probability of being nucleated to crystallize. At the interface of an ordered solid substrate and a disordered immiscible immersion fluid (electrolyte), liquid sulfur's contact angle is determined by the interfacial energies γ between these three phases: $\gamma_{solid-electrolyte}$, $\gamma_{solid-sulfur}$, $\gamma_{sulfur-electrolyte}$. Mathematically, the contact angle θ is determined by Young's equation

$$\cos\theta = \frac{\gamma_{solid-electrolyte} - \gamma_{solid-sulfur}}{\gamma_{sulfur-electrolyte}}.$$

At metal-containing solid surfaces (Fig. 2*C*), we observe that $\theta \approx 180°$, $\cos\theta \approx -1$. This extreme nonwetting condition can be achieved if $\gamma_{metal-sulfur} \approx \gamma_{sulfur-electrolyte} \gg \gamma_{metal-electrolyte}$. This is possible if there are weak interactions between liquid sulfur (nonpolar) and metal-containing solid surface (polar), and between liquid sulfur and electrolyte solution (polar), compared with relatively strong binding between solid metal and electrolyte solution. This weak interaction with solid metal and large contact angle largely isolates the liquid droplets from the electrode surface, thus minimizing heterogeneous nucleation. Compared with air as an immersion fluid, liquid electrolyte has smaller surface

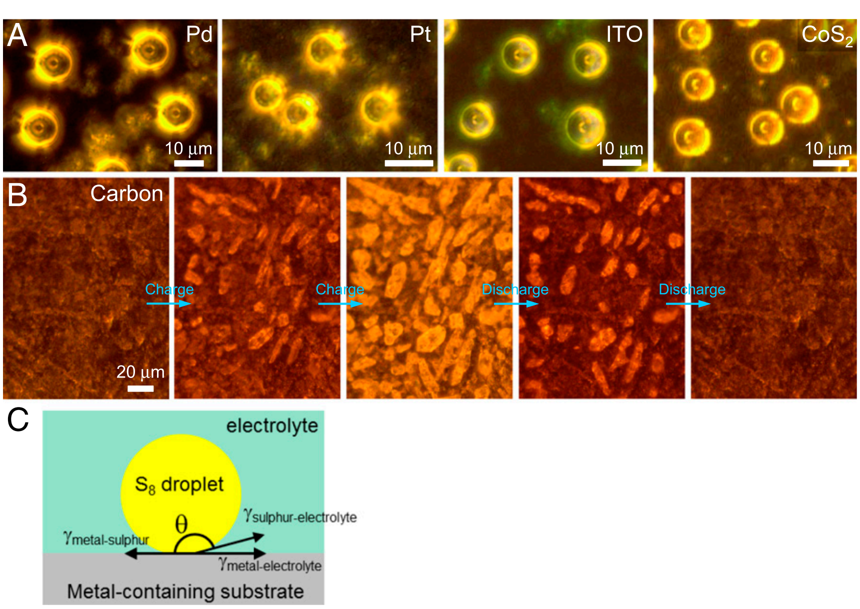

Fig. 2. Substrate-dependent electrochemical formation of supercooled sulfur at room temperature. (*A*) *In operando* DFLM images of sulfur droplets electrochemically formed on Pd, Pt, ITO, and CoS_2 substrates. (*B*) Time-lapse *in operando* DFLM images of crystalline sulfur formation and dissolution on glassy carbon substrate (see also Movie S8). (*C*) Schematic of a liquid sulfur droplet electrochemically formed on metal-containing substrate showing the quantities in Young's equation.

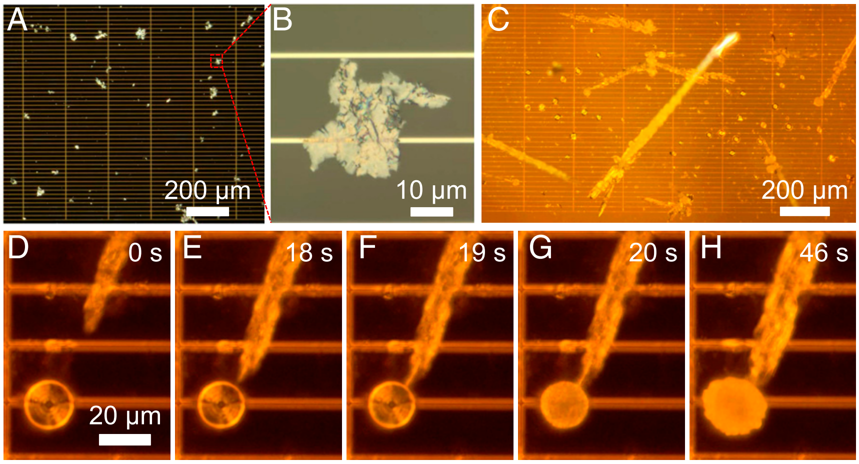

Fig. 3. Rapid solidification of a supercooled sulfur droplet touched by crystalline sulfur at room temperature. (*A*) DFLM image of exfoliated graphite nanoplatelets dispersed on Ni metal grid for growing solid and liquid sulfur in the same cell. (*B*) High-magnification bright-field light microscopy image of a single nanoplatelet sitting on Ni grid, as shown in the red box in *A*. (*C*) *In operando* DFLM image of the cell after charging, showing coexisting needle-shaped sulfur microcrystals and metastable sulfur droplets. (*D*–*H*) Time-lapse DFLM images showing the approaching of a needle-shaped sulfur microcrystal toward a sulfur microdroplet and its rapid solidification upon touching. (Scale is identical in *D*–*H*.)

energy with both metal-containing solid substrate and sulfur and contributes to the large contact angle. At a glassy carbon surface, on the other hand, the interaction between sulfur and sp^2 carbon is so strong (31) that sulfur wets carbon and easily solidifies.

Supercooled liquids usually solidify quickly after the onset of nucleation. The electrochemically generated supercooled sulfur droplets do not solidify by themselves over an observation window of 1 h. We induced nucleation at the microscale, to verify their metastability. We spread exfoliated graphite nanoplatelets on Ni metal grids (Fig. 3 *A* and *B*) to electrochemically generate both sulfur droplets and crystals in one cell (Fig. 3*C* and Movie S9) and recorded events when a sulfur crystal grown from graphite touches a sulfur droplet grown on Ni. As shown in the time-lapse images in Fig. 3 *D*–*H* extracted from Movie S10, the sulfur microdroplets turned from transparent to frosted within 1 s upon the touch of a growing sulfur microcrystal, indicating the solidification of the sulfur droplet. The rapid solidification preserved the spherical shape of the sulfur droplet (Fig. 3*G*). Upon further growth (Fig. 3*H*), the surface of the sulfur particle becomes rougher, indicating its solid and polycrystalline nature. A chain of such solidification events was also observed (*SI Appendix*, Fig. S9 and Movie S11), confirming the metastability of electrochemically generated supercooled sulfur droplets. Note that trace amounts of guest species may dope inside the liquid sulfur droplets (32) and could originate from catalytic reactions of sulfur at metal-containing surfaces (21). However, the melting temperature of these solidified electrochemically generated sulfur microdroplets is similar to that of pure S_8 powders (*SI Appendix*, Fig. S10), indicating the purity of these supercooled droplets is high.

In studies of supercooled liquid states, the fractional supercooling change $(T_m - T_{sc})/T_m$, where T_m is the melting temperature, T_{sc} is the supercooling temperature, observed before the material goes through a glass "transition" (where the viscosity can increase by 15 orders of magnitude) is typically 0.3 (9). The melting temperature of sulfur is ~115 °C = 388 K. Using the electrochemical method reported here, we successfully generated supercooled sulfur microdroplets directly at −28.4 °C = 244.6 K (Fig. 4 *A* and *B*). During electrochemical oxidation, round microdroplets of sulfur formed on Au electrode (Fig. 4 *C*–*E* and Movie S12), similar to the behavior observed afterward at room temperature (Movie S13). Merging of growing droplets, a clear signature of the liquid state, was also observed (Movie S12).

The rate-limiting step of crystallization is determined by molecular-scale fluctuations needed to overcome the free-energy barrier between the initial liquid state and an embryonic crystal. A local ordering of molecules beyond some critical radius is needed to stabilize the crystalline state against thermal fluctuations that could disrupt (dissolve) the atomic-scale ordering (33). In the case of heterogeneous nucleation, the local ordering is assisted by the presence of nucleation catalysts such as trace impurities or the interface of the liquid and a solid surface. In the case of homogeneous nucleation where there is no foreign catalyst or surface interface, nucleation requires a thermal fluctuation that is large enough to create a nanoseed crystal with critical radius r^* such that seeds with $r > r^*$ are large enough to survive thermal fluctuations that would cause the nascent seed to disappear.

Using this model, Turnbull and Fischer show that the rate for homogeneous nucleation per unit volume is proportional to $A = n^* n(kT/h)\exp[-\Delta F_A/kT]$ (26), where n^* is the critical number of atoms required to create the stable embryonic nanoseeds, n is the number of atoms/volume of liquid. ΔF_A is the free energy of activation for transporting atoms across the liquid–crystal interface and was suggested to be the same magnitude as the activation energy for viscous flow. As emphasized by Turnbull (26, 34), the elimination of all nucleation catalysts in macroscopic quantity of liquid is extremely difficult. However, if microscopic droplets were studied, there is a higher probability that some of the droplets would not contain any nucleating catalysts, and the theory of homogeneous nucleation can be tested. According to the Turnbull theory, the number fraction N_F of droplets of radius R that solidify due to homogeneous nucleation should be $1 - N_F = \exp(k_D t)$, where $k_D = v_D I$, v_D is the volume of the droplet, while for heterogeneous nucleation, $1 - N_F = \exp(k_D t)$, where $k_D = a_D I_{het}$ (26, 35).

Turnbull argued that droplets that contained impurities would freeze before reaching the homogeneous nucleation temperature while the remaining droplets would all freeze within a narrow temperature window as the nucleation rate changes dramatically from very slow to very fast over this temperature range. In a previous study using six-times-distilled sulfur condensed into droplets on a glass slide, the researchers claimed to have reached the homogeneous nucleation state, even though sulfur was condensed onto a glass surface where the wetting angle was ~62°. However, between −30 and −60 °C, ~85% of the droplets remained in the liquid state, which is contrary to classical nucleation theory (27).

In our work where the wetting angle approached 180°, as noted above, none of the sulfur droplets were observed to solidify at −28 °C. Additional experiments were done at even lower temperatures, ≤−40 °C, where the actual temperature reached the lower-temperature limit of the infrared thermometer used (*SI Appendix*, Fig. S11 and Movie S14). At the lowest temperature, the droplets retain their smooth, liquid-like appearance, as opposed to images of solidified sulfur (Fig. 3 *G* and *H* and *SI Appendix*, Fig. S11), but interestingly, the few droplets that

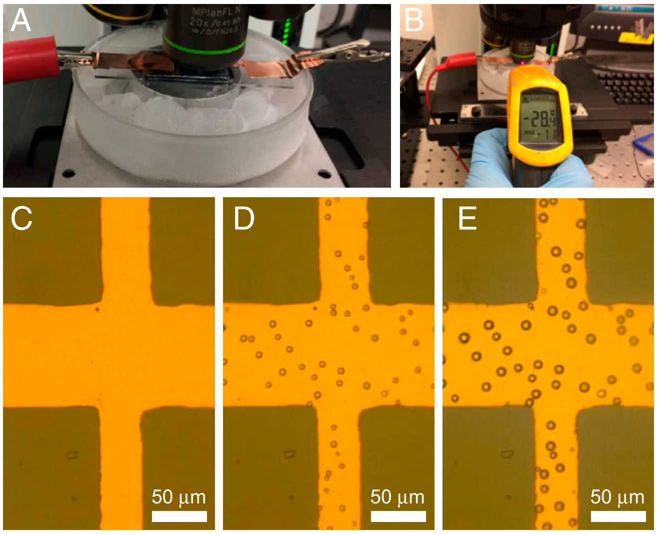

Fig. 4. Direct electrochemical generation of supercooled sulfur droplets at −28.4 °C. (*A*) Picture of a sulfur electrochemical cell in dry ice and *o*-Xylene mixture cooling bath. (*B*) Temperature at the spot of observation is measured to be −28.4 °C by an infrared thermometer. (*C*–*E*) Time-lapse light microscopy images of the formation of sulfur droplets on Au electrode at −28.4 °C.

appear to be in contact/close proximity with each other did not fuse as they did at −28.4 °C.

A possible reason may be that at these very low temperatures, the droplets may be entering into a glass transition where the viscosity η of the liquid increases exponentially with decreasing temperature $\eta(T) \sim \eta_\infty \exp(\Delta(T)/T)$, where $\Delta(T)$ is an activation energy. In so-called fragile glass formers, $\Delta(T)$ can increase significantly as T is decreased, and $\eta(T)$ can increase by more than 12 orders of magnitude over a very narrow change in temperature (9). The temperature dependence of the viscosity of liquid sulfur and supercooled sulfur measured between 155 and 80 °C was measured and shown to vary as $\eta(T) \sim \eta_\infty \exp(\Delta_0/T)$, where Δ_0 is independent of temperature (11). The extrapolation of the viscosity of liquid sulfur data discussed in ref. 11 to −40 °C gives a viscosity in the range of ∼4,000 centipoise, which is the viscosity of heavy oil to corn syrup. However, as pointed out by Kivelson and Tarjus, if the liquid material is a "fragile glass former," Δ_0 can be temperature dependent, and increase significantly with declining temperature (9). Because the movie at the coldest temperatures shows no droplets merging, this observation suggests that the supercooled sulfur may be entering into the glass transition. Clarification will need additional study.

While it is not clear whether the study of supercooled sulfur in electrolyte solution will add to deeper general understanding of supercooled liquids and the glass transition, at the very least, our work enriches lithium-sulfur-electrolyte phase diagram (36).

Besides the liquid nature of electrochemically formed sulfur, our *in operando* study also suggests the reaction pathway of sulfur nucleation and growth in Li-S batteries. While most sulfur microdroplets form on the conductive Ni line (Fig. 5*A*), we observed a few instances when they form on the insulating glass next to the Ni line (Fig. 5*B*). This suggests that sulfur could electrochemically form via a solution mechanism, in addition to the traditionally hypothesized surface mechanism. As shown in Fig. 5*C*, in the surface mechanism, polysulfide anion transfers electrons to electrode and deposits locally, whereas in the solution mechanism, electron transfer first generates soluble intermediate species which diffuse off the conducting substrate before depositing. We hypothesize the diffusive intermediate specie to be S_8 molecule, because it is slightly soluble in the DOL/DME electrolyte (37). The surface mechanism will have the issue of electrode surface being fully covered by the insulating charge/discharge product (sulfur/Li_2S) and limit the areal capacity. The solution mechanism, however, allows the product to form off the electrode surface, therefore maintains the accessibility of electrode surface to electrolyte and enables high areal capacity and rate capability (38, 39). The solution mechanism also applies to the reverse process of solid sulfur dissolution upon discharging. As shown in *SI Appendix*, Fig. S12 and Movies S15 and S16, large sulfur crystals dissolved isotropically, regardless of the accessibility of electron. And, after they broke into segments, the electrically disconnected sulfur still reacted. This finding contradicts the common belief in Li-S battery that for insulating sulfur to be electrochemically active, it needs to have small size and be electrically connected to current collector (40).

We attribute the discovery of metastable supercooled sulfur in electrochemical cell to the gentle, *in operando*, and label-free imaging technique we use. Compared with ex situ electron microscopy, *in operando* DFLM offers dynamic and true color information in the native volatile liquid electrolyte (*SI Appendix*, Fig. S13). And, the spatially patterned electrode on glass makes it possible to reveal the sulfur formation pathway (Fig. 5). This way of producing supercooled sulfur directly at low temperature with spatial, temporal, and size control provides a powerful platform to study and utilize the supercooling phenomenon.

Methods

***In Operando* Cell Fabrication.** *In operando* cells with metal substrates were fabricated on standard glass slides (25 mm × 75 mm × 1 mm). Glass slides were cleaned with soap, rinsed with water, and blow dried to remove the grease and particulates on the surface. Thermal evaporation was done with

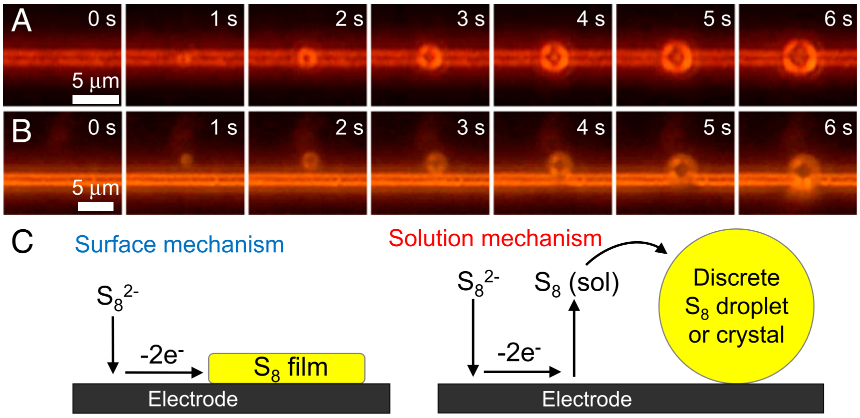

Fig. 5. Initial formation of discrete sulfur droplets on and off the conductive grid and its implication on the mechanism of Li-S battery. (*A* and *B*) Time-lapse light microscopy images of the initial formation of sulfur droplets, one on the Ni grid (*A*) and another off the Ni grid on glass (*B*). The reverse process (sulfur dissolution) is shown in *SI Appendix*, Fig. S12. (*C*) Two general mechanisms for the nucleation and growth of sulfur on electrodes. The solution mechanism is consistent with the results in both *A* and *B*.

a mask to create flat metal strips (1 mm wide, 50 nm thick) on the glass slides. To create metal microgrids, e-beam lithography was done before metal thermal evaporation, using poly(methyl methacrylate) resist on top of anticharging conductive polymer layer (Espacer, 300Z). Lithium metal was cold pressed into Ni mesh (50 μm thick; Dexmet Corp.) as the counter electrode, which was then sealed between a cover glass and the glass slide with evaporated metal electrode, using hot melt sealing film (Meltonix 1170–60; Solaronix), leaving two little openings for liquid electrolyte filling. There is an ∼50-μm gap between the top surface of the working electrode and the bottom surface of the glass coverslip, which is then occupied by electrolyte, which was 0.25 M Li_2S_8, 1 M lithium bis (trifluoromethanesulfonyl)imide (LiTFSI), and 0.1 M $LiNO_3$ dissolved in 1:1 DOL and DME. LiTFSI functions as a supporting electrolyte to enhance ionic conductivity. $LiNO_3$ passivates the Li metal surface and suppresses its reaction with polysulfide (41). After filling the electrolyte by capillary effect, the two openings were sealed using silicone vacuum grease (Dow Corning). The entire assembly of cell was done in an Ar-filled glovebox. *In operando* cells with glassy carbon substrate (Ted Pella Inc.) were assembled in pouch cells with cover-glass window.

***In Operando* Light Microscopy.** The *in operando* cells were galvanostatically cycled using an MTI 8-channel battery tester, while being imaged at the same time using a light microscope equipped with reflected dark-field illumination (BX51; Olympus Inc.), with air-immersion objective (LMPLFLN-BD, 50×, N.A. 0.5, WD 10.6 mm; Olympus), broadband xenon lamp, and CMOS detector (UC50; Olympus). The image series were taken with exposure time of 0.5 ∼ 0.8 seconds per frame and frame rate of 1 frame per second. The spatial resolution of the microscope is ∼500 nm. All of the *in operando* cells were tested at room temperature unless otherwise mentioned.

Raman Spectroscopy. The sulfur droplets were characterized using the Horiba Labram HR Evolution Raman System, with 532-nm excitation, an air-immersion objective (50×, N.A. 0.75, WD 0.38 mm; Olympus), and an electron multiplying charge-coupled device (Newton, Andor). The exposure time was set to ∼10 s.

Scanning Electron Microscopy. Scanning electron microscopy (SEM) images of electrodes cycled in polysulfide-containing electrolyte were obtained to compare with optical microscopy results. Coin cells were assembled inside a glovebox using glassy carbon or nickel foil as the working electrode and Li metal as the counter/reference electrode. On each working electrode 20 μL of the same electrolyte was added. A Celgard 2400 separator was then placed over the working electrode and an additional 20 μL of blank electrolyte (containing everything except Li_2S_8) was added on top. Finally, a lithium metal foil was placed on the separator as the anode. Galvanostatic cycling measurements were evaluated with an Arbin battery cycler. The cells were cycled between 1.0 and 2.8 V at room temperature. After cycling, the cells were disassembled for SEM imaging.

ACKNOWLEDGMENTS. The high-speed microscopy experiments were done in Manu Prakash's laboratory with assistance from Arnold Mathijssen. N.L. and S.C. acknowledge support from the Moore Foundation and Stanford University. The work was supported by the Assistant Secretary for Energy Efficiency and Renewable Energy, Office of Vehicle Technologies of the US Department of Energy under the Battery Materials Research Program and the Battery500 Consortium. The nanofabrication part was supported by the Department of Energy, Office of Basic Energy Sciences, Division of Materials Science and Engineering, under Contract DE-AC02-76SF00515.

1. Burke MJ, Gusta LV, Quamme HA, Weiser CJ, Li PH (1976) Freezing and injury in plants. *Annu Rev Plant Physiol* 27:507–528.
2. Duman JG (2001) Antifreeze and ice nucleator proteins in terrestrial arthropods. *Annu Rev Physiol* 63:327–357.
3. Gamalski AD, Tersoff J, Sharma R, Ducati C, Hofmann S (2010) Formation of metastable liquid catalyst during subeutectic growth of germanium nanowires. *Nano Lett* 10:2972–2976.
4. Berendsen TA, et al. (2014) Supercooling enables long-term transplantation survival following 4 days of liver preservation. *Nat Med* 20:790–793.
5. Çınar S, Tevis ID, Chen J, Thuo M (2016) Mechanical fracturing of core-shell undercooled metal particles for heat-free soldering. *Sci Rep* 6:21864, and erratum (2016) 6: 25218.
6. Stillinger FH (1995) A topographic view of supercooled liquids and glass-formation. *Science* 267:1935–1939.
7. Debenedetti PG, Stillinger FH (2001) Supercooled liquids and the glass transition. *Nature* 410:259–267.
8. Debenedetti PG (2003) Supercooled and glassy water. *J Phys Condens Matter* 15: R1669–R1726.
9. Kivelson SA, Tarjus G (2008) In search of a theory of supercooled liquids. *Nat Mater* 7: 831–833.
10. Andrikopoulos KS, Kalampounias AG, Falagara O, Yannopoulos SN (2013) The glassy and supercooled state of elemental sulfur: Vibrational modes, structure metastability, and polymer content. *J Chem Phys* 139:124501.
11. Fanelli R (1945) Supercooled sulfur and its viscosity. *J Am Chem Soc* 67:1832–1834.
12. Sellberg JA, et al. (2014) Ultrafast X-ray probing of water structure below the homogeneous ice nucleation temperature. *Nature* 510:381–384.
13. Handa YP, Klug DD (1988) Heat capacity and glass transition behavior of amorphous ice. *J Phys Chem* 92:3323–3325.
14. Lin C, et al. (2017) A metastable liquid melted from a crystalline solid under decompression. *Nat Commun* 8:14260.
15. Riechers B, Wittbracht F, Hütten A, Koop T (2013) The homogeneous ice nucleation rate of water droplets produced in a microfluidic device and the role of temperature uncertainty. *Phys Chem Chem Phys* 15:5873–5887.
16. Benmore CJ, Weber JKR (2017) Aerodynamic levitation, supercooled liquids and glass formation. *Adv Phys X* 2:717–736.
17. Schülli TU, et al. (2010) Substrate-enhanced supercooling in AuSi eutectic droplets. *Nature* 464:1174–1177.
18. Ji X, Lee KT, Nazar LF (2009) A highly ordered nanostructured carbon-sulphur cathode for lithium-sulphur batteries. *Nat Mater* 8:500–506.
19. Manthiram A, Fu Y, Chung SH, Zu C, Su YS (2014) Rechargeable lithium-sulfur batteries. *Chem Rev* 114:11751–11787.
20. Seh ZW, Sun Y, Zhang Q, Cui Y (2016) Designing high-energy lithium-sulfur batteries. *Chem Soc Rev* 45:5605–5634.
21. Babu G, Ababtain K, Ng KYS, Arava LMR (2015) Electrocatalysis of lithium polysulfides: Current collectors as electrodes in Li/S battery configuration. *Sci Rep* 5:8763.
22. Jiang J, et al. (2015) Encapsulation of sulfur with thin-layered nickel-based hydroxides for long-cyclic lithium-sulfur cells. *Nat Commun* 6:8622.
23. Mehdi BL, et al. (2015) Observation and quantification of nanoscale processes in lithium batteries by operando electrochemical (S)TEM. *Nano Lett* 15:2168–2173.
24. Hagen M, et al. (2013) In-situ Raman investigation of polysulfide formation in Li-S cells. *J Electrochem Soc* 160:A1205–A1214.
25. Pound GM, Mer VKL (1952) Kinetics of crystalline nucleus formation in supercooled liquid tin. *J Am Chem Soc* 74:2323–2332.
26. Turnbull D (1952) Kinetics of solidification of supercooled liquid mercury droplets. *J Chem Phys* 20:411–424.
27. Hamada S, Nakazawa YST (1970) Nucleation in liquid sulfur droplets. *Bull Chem Soc Jpn* 43:3780–3786.
28. Ward AT, Myers MB (1969) An investigation of the polymerization of liquid sulfur, sulfur-selenium, and sulfur-arsenic mixtures using Raman spectroscopy and scanning differential calorimetry. *J Phys Chem* 73:1374–1380.
29. Sun J, et al. (2014) Liquid-like pseudoelasticity of sub-10-nm crystalline silver particles. *Nat Mater* 13:1007–1012.
30. Perez M (2005) Gibbs-Thomson effects in phase transformations. *Scr Mater* 52: 709–712.
31. Zhang Q, et al. (2015) Understanding the anchoring effect of two-dimensional layered materials for lithium-sulfur batteries. *Nano Lett* 15:3780–3786.
32. Meyer B (2013) *Sulfur, Energy, and Environment* (Elsevier, Amsterdam).
33. Turnbull D, Fisher JC (1949) Rate of nucleation in condensed systems. *J Chem Phys* 17: 71–73.
34. Turnbull D (1950) Formation of crystal nuclei in liquid metals. *J Appl Phys* 21: 1022–1028.
35. Cormia RL, Price FP, Turnbull D (1962) Kinetics of crystal nucleation in polyethylene. *J Chem Phys* 37:1333–1340.
36. Dibden JW, Smith JW, Zhou N, Garcia-Araez N, Owen JR (2016) Predicting the composition and formation of solid products in lithium-sulfur batteries by using an experimental phase diagram. *Chem Commun (Camb)* 52:12885–12888.
37. Mikhaylik YV, et al. (2010) High energy rechargeable Li-S cells for EV application: Status, remaining problems and solutions. *ECS Trans* 25:23–34.
38. Yuan Z, et al. (2016) Powering lithium-sulfur battery performance by propelling polysulfide redox at sulfiphilic hosts. *Nano Lett* 16:519–527.
39. Pang Q, Kundu D, Cuisinier M, Nazar LF (2014) Surface-enhanced redox chemistry of polysulphides on a metallic and polar host for lithium-sulphur batteries. *Nat Commun* 5:4759.
40. Bruce PG, Freunberger SA, Hardwick LJ, Tarascon J-M (2011) Li-O2 and Li-S batteries with high energy storage. *Nat Mater* 11:19–29.
41. Aurbach D, et al. (2009) On the surface chemical aspects of very high energy density, rechargeable Li–Sulfur batteries. *J Electrochem Soc* 156:694–702.